Solar Energy 240 (2022) 290–300

Contents lists available at ScienceDirect

Solar Energy

journal homepage: www.elsevier.com/locate/solener

# Experimental study on the blocking effect of metal mesh on seepage of molten salt in tank foundation materials

Mingrui Zhang [a,b], Yuhang Zuo [a], Ao Zhang [a], Hao Zhou [a,*]

[a] State Key Laboratory of Clean Energy Utilization, Institute for Thermal Power Engineering, Zhejiang University, Hangzhou 310027, China
[b] Polytechnic Institute, Zhejiang University, Hangzhou 310027, China

ARTICLE INFO

*Keywords:*
Concentrating solar power
Molten salt
Storage tank leakage
Seepage and blocking

ABSTRACT

Leakage of molten salt storage tanks in concentrated solar power plants poses a major threat to operating safety. This paper focuses on arranging metal mesh in the storage tank foundation to control the seepage and migration range of molten salt in the thermal-steady foundation materials after leakage occurs. The influences of different conditions, including the metal mesh aperture, metal mesh position, operating temperature, and the mass of leaked molten salt, on the blocking effect were investigated through a custom-built experimental system that modeled the actual leaking process. The results showed that the metal mesh can effectively block seepage of molten salt. When the metal mesh aperture is made smaller or the mesh is placed further toward the bottom of the tank, the metal mesh has a significant blocking effect on molten salt seepage. Especially when the metal mesh aperture is 0.15 mm and the depth of placement is 325 mm, seepage of molten salt can be completely blocked. Nevertheless, it has been found that the depth of molten salt seepage distinctly increases with higher operating temperature or larger leaked molten salt mass. These experimental results will provide references for pollution control and disposition of molten salt leakage accidents and help power plant engineers re-examine tank foundation designs.

## 1. Introduction

Energy and the environment are currently the two major themes of human social development. With rapid economic growth, traditional fossil energy consumption is increasing day by day. The greenhouse effect caused by the accompanying carbon emissions significantly impacts the human living environment. The large-scale application of renewable energy is critical to reducing carbon dioxide and plays a significant role in the complex process by which human beings can achieve "carbon neutrality" (Juan lin et al., 2021; Wan et al., 2021). Concentrating solar power (CSP) is a form of renewable energy generation that has attracted much attention in recent decades because it produces almost no pollution or greenhouse gases during power generation (Kannan and Vakeesan, 2016; Peinado Gonzalo et al., 2019). In 2017, the government of China announced the first batch of 20 CSP demonstration projects with a total capacity of 1349 MW (Lovegrove and Stein, 2021). As of January 2021, seven demonstration projects have been put into operation. In October 2021, the "Carbon Peak Action Plan by 2030″ drawn up by the State Council of China also clearly pointed out the active development of concentrating solar power.

The thermal energy storage (TES) system is one of the core systems in the regular operation of CSP plants. The foundation of the storage tank is an essential part of the system, which plays a role in supporting the tank body, insulating the molten salt storage tank, preventing the molten salt from cooling and solidifying, and preventing the over-temperature of the concrete building structure. Several researchers have studied the thermal characteristics of the foundation. Rodríguez et al. (2013) proposed a parallel and modular object-oriented modeling method that treats different elements of molten salt storage tanks as independent systems. The foundation of the molten salt storage tank consists of a foam glass insulation layer, a passive cooling system, and a reinforced concrete layer that can only withstand temperatures below 90 °C. Torras et al. (2015) concluded that to reduce the heat exchange loss between the molten salt and the external environment, the insulation thickness of the storage tank is an essential design parameter. When designing the storage tank, it is critical to consider that the foundation's configuration and size will have a significant influence on the ambient temperature around the storage tank. Zhou et al. (2020b) used experimental and numerical methods to study the temperature distribution and heat loss of storage tank foundations at different scales. A new type of multi-layer foundation structure was proposed to insulate the foundation and was

* Corresponding author at: State Key Laboratory of Clean Energy Utilization, Zhejiang University, Zheda Road 38, Hangzhou 310027, China.
*E-mail address:* zhouhao@zju.edu.cn (H. Zhou).

https://doi.org/10.1016/j.solener.2022.05.047
Received 11 January 2022; Received in revised form 18 May 2022; Accepted 24 May 2022
Available online 30 May 2022

**Nomenclature**

| | |
|---|---|
| $D_0$ | Seepage depth of molten salt without metal mesh (mm) |
| $D_1$ | Distance between the top of the solid block and the top of LECA (mm) |
| $D_2$ | Seepage depth of molten salt with metal mesh (mm) |
| $M_1$ | Mass of solid block (g) |
| $M_2$ | Mass of LECA adsorbed per unit mass of molten salt |
| $M_{le}$ | Mass of leaked molten salt (g) |
| $S$ | Metal mesh aperture (mm) |
| $T$ | Temperature (°C) |
| $T_{op}$ | Operating temperature of the resistance heater (°C) |
| $t$ | Time (s, min, h) |
| $W_0$ | Maximum seepage width of molten salt without metal mesh (mm) |
| $W$ | Maximum seepage width of molten salt with metal mesh (mm) |
| $Y$ | Metal mesh position (mm) |
| $y$ | Vertical coordinate (mm) |
| $\varepsilon$ | Interception rate |
| $\sigma$ | Diffusion rate |

applied to the foundation of a 1 MWth pilot platform to prove the practicality and prospects of its industrial application.

Due to the influence of gravity of molten salt, alternating thermal stress of tanks (Flueckiger et al., 2011; Wan et al., 2020), long-term corrosion by high-temperature molten salt (Fernández et al., 2012; Gomes et al., 2019; Villada et al., 2021; Zhang et al., 2020), poor weld bad quality or poor corrosion resistance of the flux material, the molten salt storage tanks may rupture, causing leakage accidents. In the event of a leakage accident, repairing the tanks has required delays that have significantly degraded plant availabilities. In addition, salt that leaks into the foundation can increase thermal losses, cause overheating of the foundation and produce $NO_x$ (Price et al., 2021). A tank leak occurred in the Crescent Sand Dune CSP in the United States in 2016, and the plant was shut down for eight months. The loss of electricity sales revenue caused by the one-month outage was about 4 million US dollars. To prevent molten salt tank leakage, some researchers have taken the mechanical performance of the tank as a starting point for problem-solving. Wang et al. (2020) found that the maximum mechanical stress on the steel wall can be decreased by increasing the inlet molten salt velocity, the cold molten salt temperature, or the firebrick thickness, or by decreasing the steel wall thickness, the porosity of the porous bed, the diameter, the thermal conductivity or the specific heat of solid filler particle. Wang et al. (2021) presented an effect evaluation of the initial hot molten salt temperature on the behaviors of a thermally stratified tank, and concluded that a higher initial hot molten salt temperature can reduce the total heat storage duration of the tank, but can increase the peak maximum mechanical stress of the tank. Because of the combined effect of many factors involved in leakage, the above research cannot completely eliminate safety hazards, and tank leakage may still occur. Therefore, it is also very important to deal with the work of controlling leaks after a leakage accident.

The seepage of molten salt into the tank foundation after leakage is essentially the process of fluid seepage in porous media. Research into this process can help us better understand and deal with accidents. In a study of seepage and migration in porous media, Qi et al. (2018) used the Lattice Boltzmann Method (LBM) to simulate the mesoscopic migration of oil and water in porous media. They analyzed the velocity and pressure distribution law of oil and water and then obtained the fitting equation of the resistance coefficient of oil and water with varying porosity. Huang et al. (2020) selected a light non-aqueous phase liquid (LNAPL) as a diesel tracer to conduct an experimental study on seepage and migration of pollutants in fractured porous media. The results showed seepage and migration of pollutants due to fractures. The dominant flow in fractured media was more evident than in porous media. Feng et al. (2020) used computational fluid dynamics and discrete element methods to study the migration of particles in porous media. They observed that the behavior of suspended particles is mainly controlled by particle size due to particle repulsion and bridging. As the particle concentration increases, the particles occupy more of the pore space, so that the permeability of the porous medium gradually decreases.

Unlike above-mentioned fluid seepage and migration, the seepage and migration of molten salt into the tank foundation are also accompanied by a phase change in molten salt. Related research is relatively scarce for such complex fluid mechanics and heat transfer problems. Wu et al. (2017) used the fluid volume model to study numerically the phase change phenomenon and the seepage and migration characteristics of molten salt in the porous soil system. It was found that the largest radius and depth occur during migration due to solidification of molten salt. As the inlet temperature increases, both the maximum radius and depth increase. However, the increase in inlet velocity is accompanied only by an increase in the maximum migration radius. Zhang et al. (2019) conducted experimental and numerical studies on migration and solidification of molten salt in a cold porous system containing sand particles. The results showed that the molten salt continued to migrate after being poured into the porous medium and that a transparent liquidus molten salt appeared during the discharge stage. The layer was then cured into a white opaque solid block after discharge. The simulation results were in good agreement with experimental results. Wang et al., (2022) used the Moving Particle Semi-implicit (MPS) method to simulate migration and solidification behavior. They found that heat transfer in the melt is jointly determined by the two heat transfer modes of flow heat transfer and solid heat transfer. Note that the actual storage tank foundation is affected by the temperature of the storage tank, forming a stable temperature field, and is not a simple cold porous medium. Zhou et al. (2020a) noticed this and studied a series of influencing factors on leakage by designing an experimental system of their own. These results can help power plant staff better understand the flow of molten salt in the foundation after a tank leakage accident and to effectively deal with the accident.

In summary, a few researchers have studied seepage and migration of molten salt in cold and hot porous media, but the process of seepage and migration into the tank foundation after molten salt leakage has only advanced to the study of characteristics. How to conduct molten salt seepage research on blocking and preventing the further expansion of accidental pollution has not been reported yet. It is easy to think that a flat sheet can be laid in the tank foundation to block the seepage of molten salt. Nevertheless, installing the flat sheet in the tank foundation is inconvenient, and the cost is high. In addition, the flat sheet will cause excessive radial migration of molten salt after leakage. When the molten salt is in contact with the inner wall of the foundation in the radial seepage, it will adhere tightly to the inner wall of the foundation after solidification, which increases the difficulty of accident response. Using the metal mesh instead of the flat sheet can not only solve the problem of installation and cost, but also control the radial and axial migration of molten salt within an acceptable range, which is a technical means with more engineering application prospects. In this paper, a method of arranging a metal mesh instead of a flat sheet in the foundation to block the seepage of molten salt was proposed. An experimental study was carried out on blocking the seepage and migration of molten salt in the foundation. The impact of metal mesh aperture, metal mesh position, storage tank operating temperature, and leaked mass was discussed. The results obtained from this study will be useful for engineering design of a protective device to stop molten salt seepage and reduce the economic loss and safety risks of leakage accidents.

## 2. Experimental system and methods

### 2.1. Experimental materials

The molten salt used in the experiments was Solar Salt, which is currently commercially available. It was provided by Zhejiang Lianda Chemical Co. Ltd., with a purity of over 99.5%. The molten salt is a mixture of 60 wt% $NaNO_3$ and 40 wt% $KNO_3$, and its properties are shown in Table 1 (Chieruzzi et al., 2017; Dunn et al., 2012). The metal mesh is made of 304 stainless steel, which can effectively resist high temperatures and is inexpensive. The metal mesh will not affect the overall structure of the tank foundation. The metal mesh apertures are 1.6, 0.8, 0.43, and 0.15 mm, as shown in Fig. 1.

Because over-temperature of the concrete layer at the bottom of the tank foundation will reduce strength and cause cracks, which will endanger the overall structure, the foundation materials of the storage tank must have good thermal insulation properties. Light expanded clay aggregate (LECA) (Bonilla et al., 2018) has the characteristics of light weight, low thermal conductivity of about 0.113 W/(m • K) and excellent thermostability under high-temperature conditions (up to 1000 °C) (Zhou et al., 2020c), which can meet the thermal insulation requirements. In this study, LECA with mixed particle sizes were used as foundation materials for the investigation of molten salt leaking. The seepage and migration characteristics of molten salt in the LECA after leakage were obtained. The related properties of LECA are shown in Table 2 (Zhou et al., 2020a).

### 2.2. Experimental system

To model the seepage of molten salt into the tank foundation materials after leaking from storage tanks, a leakage and seepage experimental system of the molten salt was built, as shown in Fig. 2. The experimental system was mainly composed of a test rig, resistance heater, temperature control instrument, lifting device, muffle furnace, computer, data acquisition instrument, and thermocouples.

The muffle furnace heated the molten salt used in the experiment to the required temperature. The complex molten salt storage tank was replaced by an electrical resistance heater with a temperature control range from 30 °C to 800 °C, which implemented the thermal effect of the high-temperature molten salt in the tank on the foundation materials. The test rig had a cylindrical shape with an inner diameter of 345 mm and a depth of 760 mm, and the height of the heater was 60 mm. The interior of the test rig was filled with LECA to model the tank foundation materials, where a metal mesh was previously set. The walls of the test rig and the electrical resistance heater were insulated with refractory bricks and aluminosilicate fiber cotton to reduce heat dissipation during the experiment. The bottom tray of the test rig could be opened to discharge the foundation filling materials. A total of 15 K-type thermocouples were arranged every 40 mm along the axial direction of the tank center with an accuracy of ± 1 °C. The thermocouples measured the temperature change and distribution of the foundation materials during the experiment. All the thermocouples were connected to the data acquisition instrument, and the data were read and saved by the computer.

**Table 1**
Properties of Solar Salt (Chieruzzi et al., 2017; Dunn et al., 2012).

| Property | Unit | Value ( T, °C ) |
|---|---|---|
| Melting point | °C | 220.85 |
| Freezing point | °C | 237.85 |
| Latent heat | kJ/kg | 113.03 |
| Specific heat | J/(kg •°C) | 1443 + 0.172 • T |
| Density | kg/m$^3$ | 2090–0.636 • T |
| Thermal conductivity | W/(m • K) | 0.443 + 0.00019 • T |
| Dynamic viscosity | Pa • s | $2.2714 \cdot 10^{-2} - 1.2 \cdot 10^{-4} \cdot T + 2.281 \cdot 10^{-7} \cdot T^2 - 1.474 \cdot 10^{-10} \cdot T^3$ |

### 2.3. Experimental methods

As shown in Fig. 3, the experimental procedure included molten salt pretreatment, foundation materials heating, molten salt leakage, and molten salt seepage and phase change processes.

1) First, the salt was heated in a dryer at 110 °C for 5 h as a drying treatment, the required mass of salt was weighed, the heating program of the muffle furnace was set, and the crucible containing salt was placed in the muffle furnace.
2) The resistance heater was then pulled up, the foundation materials were poured into the tank, the metal mesh was placed in the position corresponding to the experimental case, and the heater was lowered back into place. The resistance heater was turned on, and the foundation was heated until its temperature reaches a steady state.
3) The resistance heater was then lifted up, the crucible containing the molten salt was removed from the muffle furnace, and the molten salt was poured into the foundation materials at the central position. The heater was then quickly lowered.
4) The heater temperature was continually maintained, and the heater was turned off after the foundation reached a new steady state.

After the foundation had cooled, the bottom tray was opened to discharge the LECA. The solid block was supported in the test rig by thermocouples so that it would not fall off with the LECA. Fig. 4 presents a schematic diagram of the experimental measurement. The distance between the top of the solid block and the top of the LECA, $D_1$, and the seepage depth of molten salt, $D_2$, were obtained when the solid block was in the test rig. If the thermocouples were unplugged and the solid block removed, the maximum seepage width of molten salt, $W$, and the mass of the solid block, $M_1$, could be measured.

Table 3 shows the experimental cases. The tests in cases A-A4 addressed the effect of the metal mesh aperture $S$ on the blocking effect. Compared with case A1, cases B1 and B2 had different metal mesh positions $Y$. Moreover, compared with case B2, cases C1 and C2 had different operating temperatures $T_{op}$. The tests in cases C1, E1, and E2 addressed the effect of the mass of leaked molten salt, $M_{le}$.

## 3. Results and discussion

### 3.1. Temperature evolution and distribution

Before discussing the blocking effect of the metal mesh on the molten salt seepage, the temperature evolution and distribution in the test rig during the experiment must be described. The temperature evolution and distribution of basic case A is shown in Fig. 3, where the operating temperature $T_{op}$ was 550 °C, and the mass of leaked molten salt $M_{le}$ was 450 g. The temperature evolution in the foundation materials can be divided into three stages: heating, leaking, and cooling. These three stages also correspond to the high-temperature molten salt filling process of the storage tank, the molten salt seepage process after a leakage accident, and the cooling process of the storage tank when stopping operation. During heating, the foundation temperature rises rapidly in the first 400 min, followed by a slower temperature rise, and finally a steady state after about 24 h. During leakage, the temperature rises sharply at the beginning because the high-temperature molten salt seeps into the foundation material from top to bottom due to the action of gravity. Then the temperature decreases and finally becomes stable after 12 h. During cooling, the temperature decreases rapidly, and the temperature levels off after 20 h.

Fig. 5(a) shows that at $y$ = 40 mm and $y$ = 80 mm, the steady-state temperatures were 490.2 °C and 349.7 °C respectively, which are much higher than the freezing point of molten salt. Thereby, solidification of

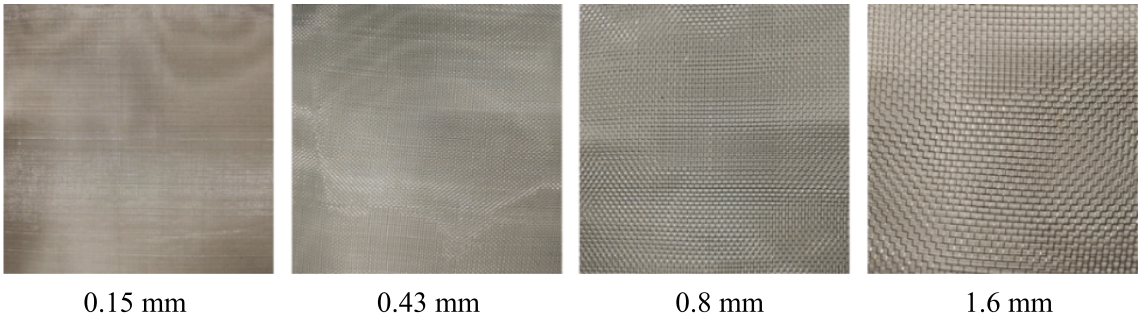


**Fig. 1.** Appearance of metal mesh.

**Table 2**
Properties of LECA (Zhou et al., 2020a).

| Property | LECA | |
|---|---|---|
| Particle sizes | 3.35–6.3 mm | 39% |
| | 6.3–8 mm | 31% |
| | 8–10 mm | 13% |
| | 10–20 mm | 17% |
| Porosity (%) | 43.3 | |
| Bulk density (kg/m$^3$) | 373.5 | |

molten salt did not occur in this area. The steady-state temperature at $y = 240$ mm was 95.7 °C, and when $y > 240$ mm, the temperature gradient was small. In the area of $y = 80$–240 mm, the molten salt began to solidify and crystallize, but due to the speed of seepage, the molten salt did not completely solidify in this area. In the area of $y > 240$ mm, the temperature of the foundation materials was much lower than the freezing point of molten salt, and the molten salt exchanged heat violently with the foundation materials in this area. The increase in solidified crystallization hindered the further downward seepage of molten salt, which finally completely solidified in this area.

Fig. 6 shows the steady-state axial temperature distribution of the foundation before and after molten salt leakage. The law that the equilibrium temperature increases as the operating temperature increases was determined first. When $T_{op}$ was 550 °C, 450 °C, and 350 °C, the foundation steady-state axial temperature after molten salt leakage increased by 7.47 °C, 7.92 °C, and 6.90 °C on average compared to the temperature before leakage. This shows that molten salt leakage had a significant effect on increasing the steady-state axial temperature of the foundation. This occurred because the thermal conductivity of the solid blocks formed by molten salt and LECA during seepage and migration was higher than that of the LECA itself (Zhou et al., 2019, 2020c). Therefore, all solid blocks must be taken out after a leakage accident occurs at a solar power plant. Failing to do so will affect the thermal insulation properties of the foundation materials and cause over-temperature damage to the concrete at the bottom of the foundation.

### 3.2. *Blocking effects under different conditions*

In blocking molten salt seepage, factors such as metal mesh aperture,

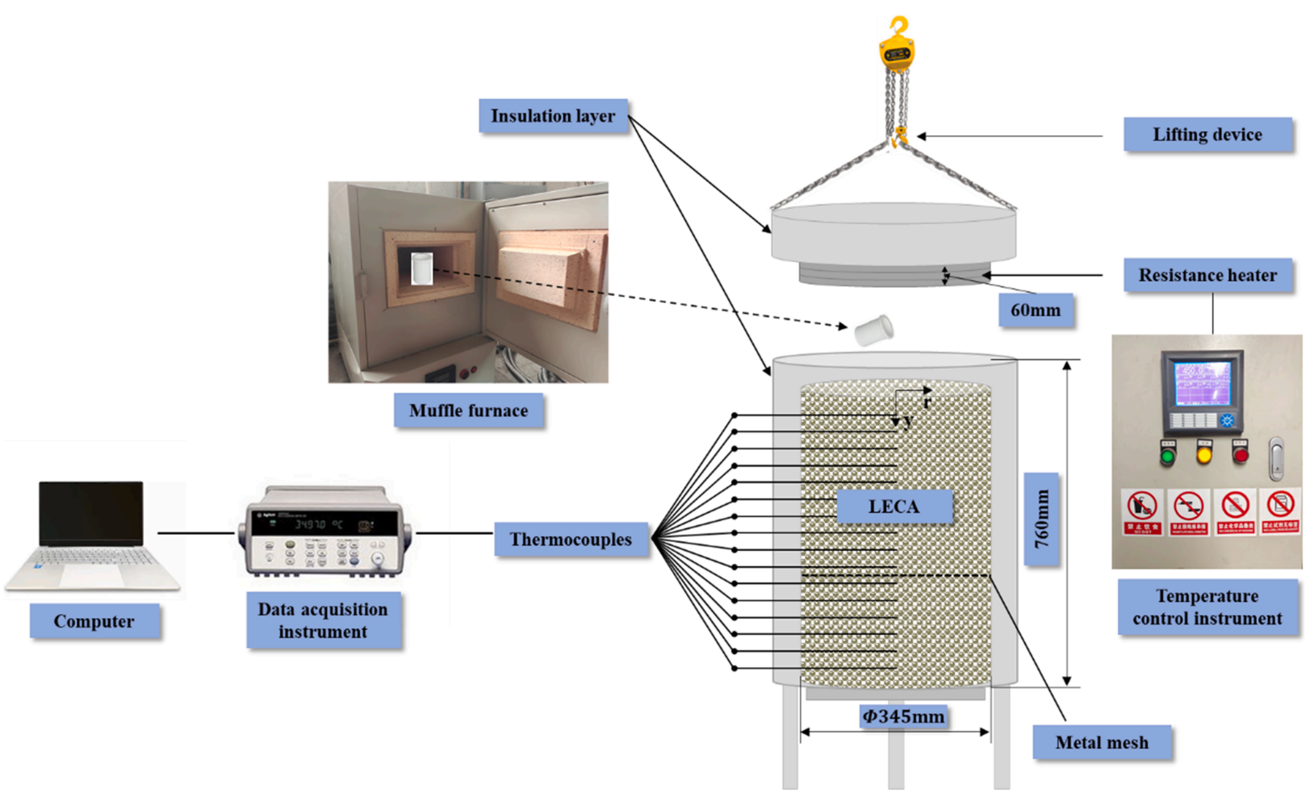


**Fig. 2.** Experimental system for molten salt seepage.

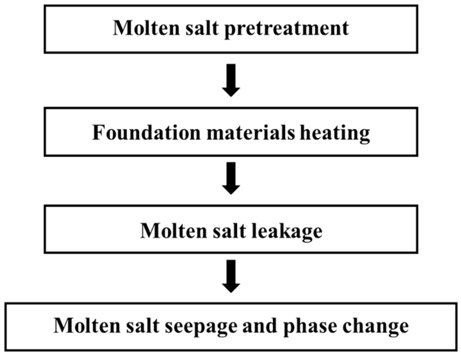


**Fig. 3.** Flow diagram of the experiment.

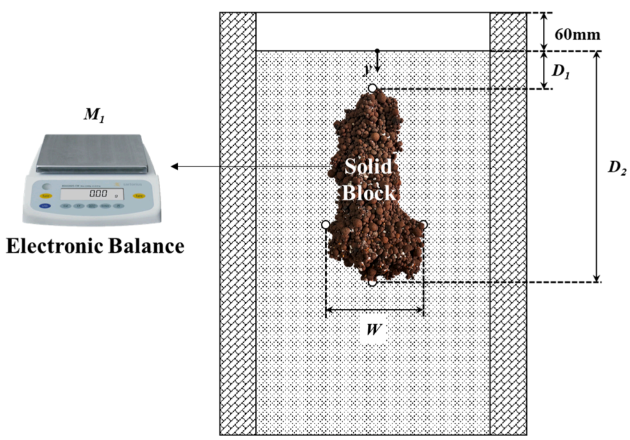


**Fig.4.** Schematic diagram of the experimental measurement.

**Table 3**
Case conditions.

| Case | Operating temperature $T_{op}$/ °C | Metal mesh position $Y$ (mm) | Metal mesh aperture $S$ (mm) | Mass of leaked molten salt $M_{le}$ (g) |
|---|---|---|---|---|
| A | 550 | / | / | 450 |
| A1 | 550 | 325 | 0.15 | 450 |
| A2 | 550 | 325 | 0.43 | 450 |
| A3 | 550 | 325 | 0.80 | 450 |
| A4 | 550 | 325 | 1.60 | 450 |
| B1 | 550 | 60 | 0.15 | 450 |
| B2 | 550 | 180 | 0.15 | 450 |
| C1 | 450 | 180 | 0.15 | 450 |
| C2 | 350 | 180 | 0.15 | 450 |
| E1 | 450 | 180 | 0.15 | 650 |
| E2 | 450 | 180 | 0.15 | 900 |

metal mesh position, operating temperature, and mass of leaked molten salt will all affect the process. Therefore, an experimental study was carried out on these influencing factors.

### 3.2.1. *Effect of metal mesh aperture on seepage and blocking*

Fig. 7 shows the foundation temperature change and distribution during molten salt leakage in case A1. It is apparent that the temperature was stable during the 0–118 s process because molten salt leakage had not yet occurred. After 118 s, the foundation temperature began to rise along the axial direction. At 134 s, the temperatures at $y = 320$ mm and above were all higher than the freezing point of molten salt, and this condition lasted until the 800 s. This shows that the molten salt was mainly maintained in a liquid state during leakage, but that the temperature rise was not detected below $y = 320$ mm, indicating that the molten salt may have not continued to seep down. This may have been due to the lower temperature at $y = 320$ mm, which was 69.2 °C. When the molten salt seeped down the position of the metal mesh, it solidified and crystallized after heat transfer with the cold LECA. Assuming that the metal mesh aperture was 0.15 mm and that the crystal size was larger, the molten salt could not have broken through the metal mesh. Instead, it accumulated on the mesh and eventually formed a solid block with LECA. Temperature change with time along the vertical direction of the foundation during seepage in case A1 is shown in Fig. 8. Note that the temperatures of the foundation below $y = 320$ mm all coincided after leakage occurred, indicating that the temperature did not change over time, which is also consistent with the seepage depth in Fig. 7. Of course, basic temperature data alone are not enough to determine whether molten salt was completely blocked under working condition A1. It is also possible that the molten salt was not in contact with the thermocouple due to the uncertainty of the downward seepage trajectory. This needs to be verified by experimental measurements.

Fig. 9 shows the effect of the metal mesh aperture $S$ on the seepage characteristics of molten salt, where the operating temperature $T_{op}$ was 550°C, the metal mesh aperture $Y$ was 325 mm, and the mass of leaked molten salt $M_{le}$ was 450 g. Case A was a comparative working condition; there was no metal mesh in the foundation, and the seepage depth $D_0$ and the maximum seepage width $W_0$ were 614 mm and 143 mm respectively. The seepage depths $D_2$ in cases A1, A2, A3, and A4 were 325, 504, 539, and 576 mm respectively. The experimental results for case A1 also confirmed the temperature evolution analysis in Fig. 7, which indicated that the molten salt was completely blocked at the metal mesh position. The maximum seepage widths $W$ were 245, 208, 158, and 144 mm, and the maximum seepage widths all occurred at the metal mesh position. This shows that the metal mesh had a certain blocking effect on molten salt seepage into the foundation and that the seepage depth decreased with reduced size of the metal mesh aperture. The maximum seepage width, however, increased at smaller metal mesh apertures. The distances between the top of the solid block and the top of the LECA ($D_1$) in cases A, A1, A2, A3, and A4 were 111, 119, 109,108, and 108 mm respectively. Clearly, there was almost no change in $D_1$. The reason for this was that the initial temperature distribution under the A series of cases was consistent, and this characteristic is highly dependent on temperature distribution.

The interception rate $\varepsilon$ is defined as the percentage decrease in seepage depth, and the diffusion rate $\sigma$ as the percentage increase in maximum seepage width after placing different metal meshes:

$$\varepsilon = (D_0 - D_2)/D_0 \times 100\% \tag{1}$$

$$\sigma = (W - W_0)/W_0 \times 100\% \tag{2}$$

As mentioned before, the function of the metal mesh is to limit the seepage range of molten salt to a reasonable range, which means to reduce the seepage depth while avoiding excessive increase in seepage width. These two parameters can help us more intuitively and accurately understand the blocking effect of metal mesh on molten salt seepage. It can be seen from Fig. 10 that the interception rates in cases A1, A2, A3, and A4 were 47.06%, 17.92%, 12.22%, and 6.19% respectively, and the diffusion rates were 71.29%, 45.42%, 10.47% and 0.73% respectively. In case A1, the 0.15-mm aperture metal mesh had the highest interception and diffusion rates for blocking molten salt. A high interception rate is beneficial to accident response. In contrast, a high diffusion rate may cause the molten salt to adhere to the inner wall of the foundation and even leak out of the foundation from the side, expanding any pollution accident. However, for case A1, the metal mesh was arranged at a deep position, so that even if the diffusion rate was large, the molten salt might not be able to leak out of the foundation.

Due to the blocking effect of the metal mesh, the solid blocks above and below the metal mesh were not tightly adhered, and the solid block section of the metal mesh layer in cases A1, A2, A3, and A4 could be easily obtained by separating the upper and lower parts and removing the metal mesh, as shown in Fig. 11. The amount of molten salt in the

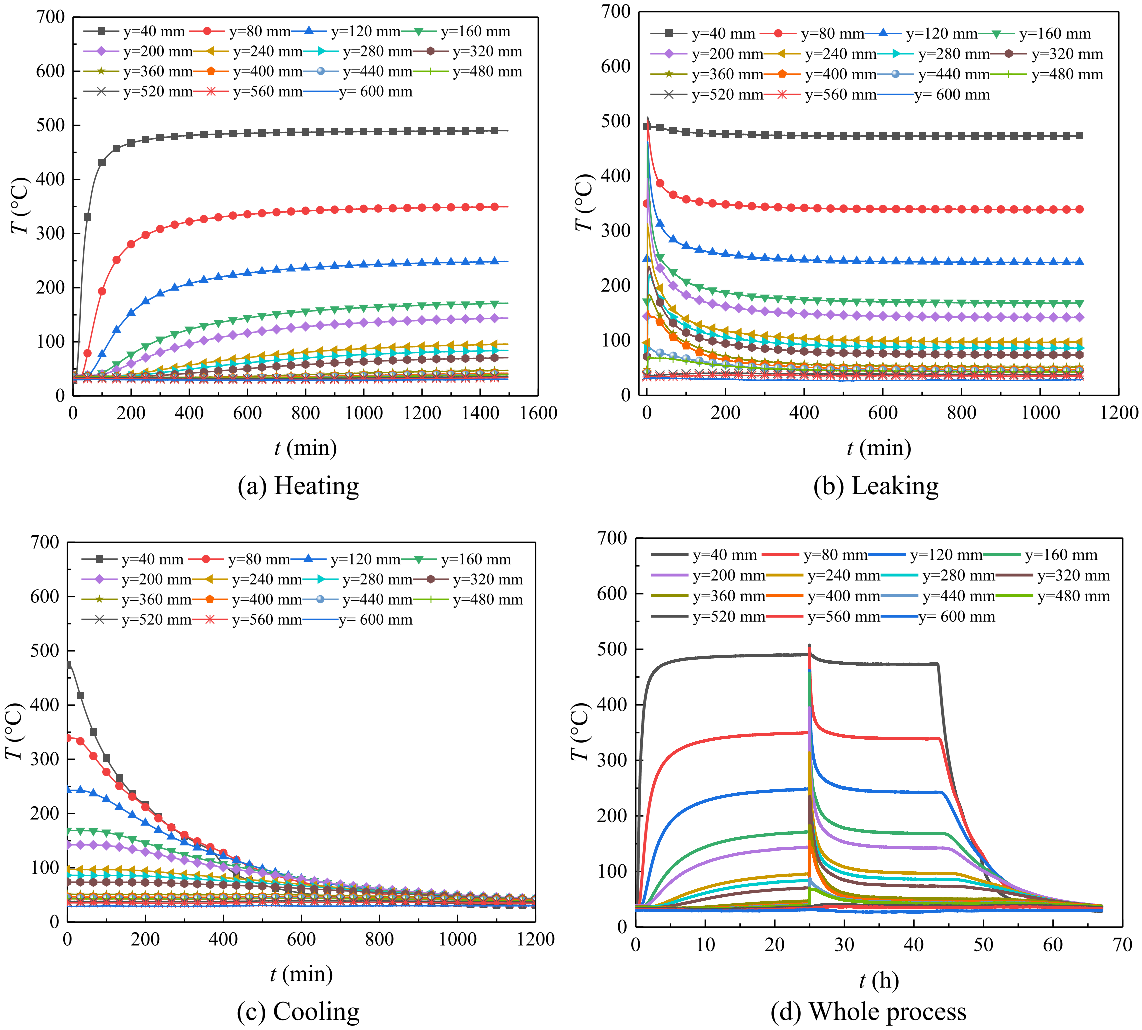


**Fig. 5.** Temperature evolution and distribution during the experiment of case A ($T_{op}$ = 550℃, $M_{le}$ = 450 g, without metal mesh).

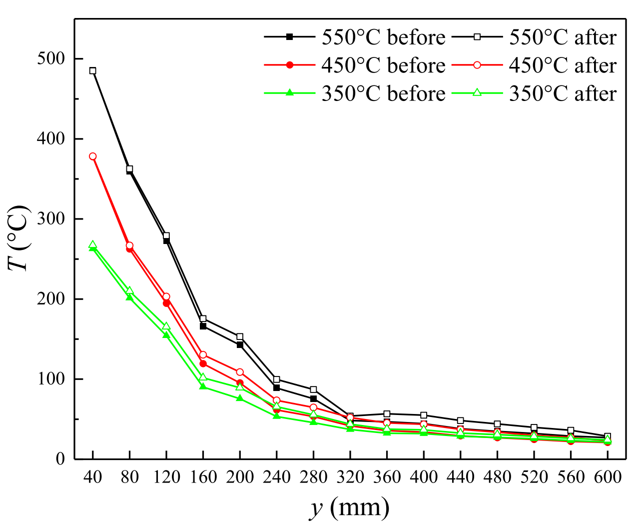


**Fig. 6.** Steady-state axial temperature distribution of the foundation at different operating temperatures before and after molten salt leakage.

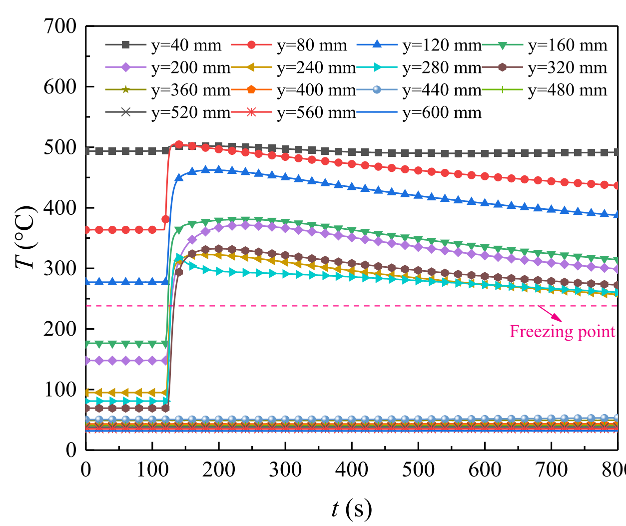


**Fig. 7.** Temperature change and distribution in the foundation under case A1 ($T_{op}$ = 550℃, $S$ = 0.15 mm, $Y$ = 325 mm, $M_{le}$ = 450 g).

solid block section of the metal mesh layer in case A1 was significantly larger than in the other cases. On the other hand, there was almost no molten salt in the solid block section of the metal mesh layer in case A4, indicating that the 1.6-mm metal mesh did not play a significant role in blocking molten salt seepage.

Fig. 12 shows the effect of metal mesh aperture on the mass of the

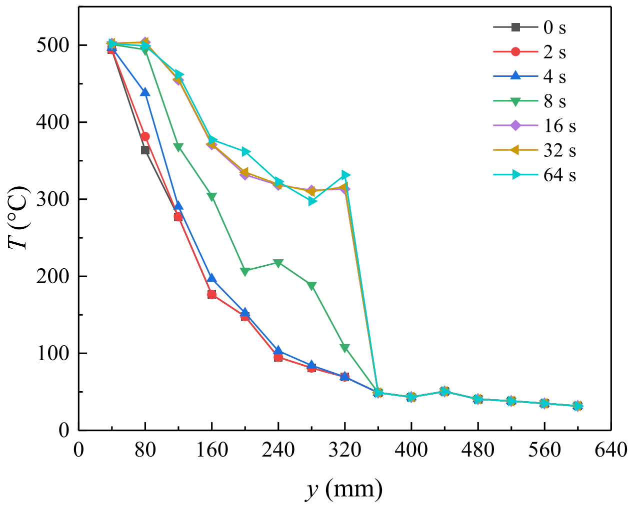


**Fig. 8.** Temperature change with time along the vertical direction of the foundation during seepage under case A1 ($T_{op}$ = 550°C, $S$ = 0.15 mm, $Y$ = 325 mm, $M_{le}$ = 450 g).

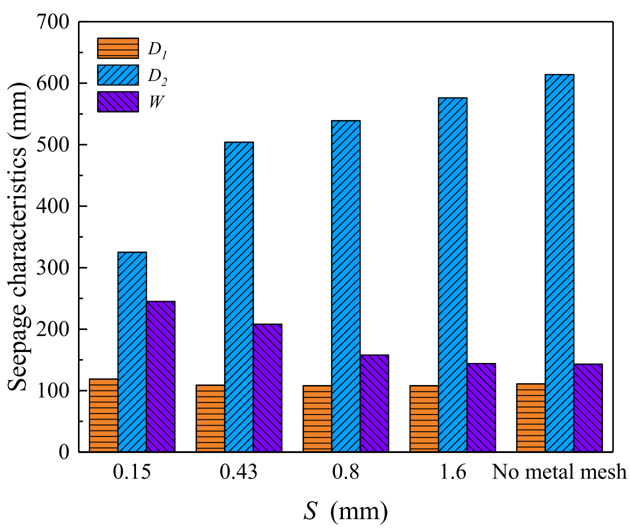


**Fig. 9.** Effect of metal mesh aperture on seepage characteristics.

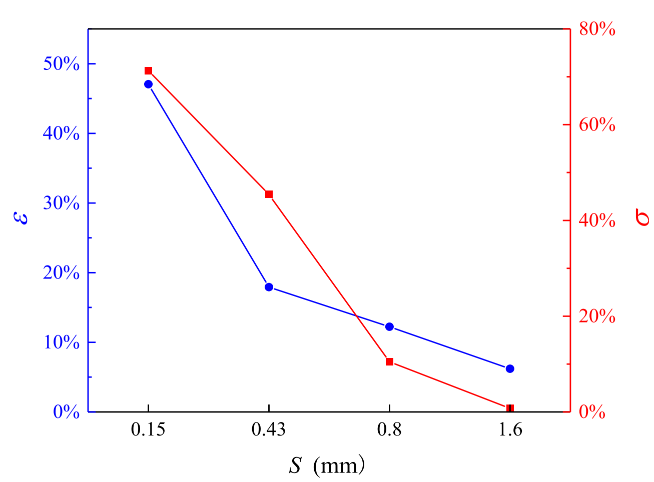


**Fig. 10.** Effect of metal mesh aperture on blocking of molten salt.

solid block. The figure shows that the masses of solid block $M_1$ in cases A1, A2, A3, and A4 were 575.1 g, 930.1 g, 1064.0 g, and 1222.2 g respectively, and that the masses of LECA adsorbed per unit mass of molten salt $M_2$ were 0.28, 1.07, 1.36, and 1.72 respectively. $M_2$ can reflect the adsorption state of molten salt on LECA during seepage. As the metal mesh aperture increases, $M_2$ decreases. This is true mainly due to the larger metal mesh aperture has a lesser blocking effect on the seepage of molten salt, and the seepage depth of molten salt increases, allowing more LECA to be adsorbed along the way. At the same time, the metal mesh in case A1 had a strong blocking effect on molten salt, and the molten salt mainly accumulated at the metal mesh position, minimizing the opportunity for molten salt to adhere to LECA. From the point of view of accident response, smaller values of $M_1$ and $M_2$ are better because the mass of solid blocks to be handled is smaller and accident response is less difficult. When metal mesh is arranged in a real tank foundation in a solar power plant, a metal mesh with smaller aperture should be selected as much as possible. However, it should also be ensured that the seepage width will not increase excessively. From the experimental results, the metal mesh with 0.15-mm aperture has an excellent control effect on the molten salt seepage range and can be considered for use.

#### 3.2.2. Effect of metal mesh position on seepage and blocking

The results in Section 3.2.1 indicate that when the mesh aperture $S$ was 0.15 mm, the metal mesh had a better blocking effect on molten salt seepage. In addition, to block molten salt from the upper portion of the foundation as much as possible, arranging the metal mesh closer to the resistance heater was considered. The effect of metal mesh position $Y$ on molten salt seepage characteristics is shown in Fig. 13, where the operating temperature $T_{op}$ was 550 °C, the metal mesh aperture $S$ was 0.15 mm, and the mass of leaked molten salt $M_{le}$ was 450 g. When $Y$ = 60 mm, $Y$ = 180 mm, and $Y$ = 325 mm, the $D_1$ values were 112, 114, and 119 mm, the molten salt seepage depths $D_2$ were 544, 531, and 325 mm, and the maximum seepage widths $W$ were 146, 177, and 245 mm respectively. When the metal mesh position was $Y$ = 60 mm, the metal mesh could not intercept molten salt above itself, and the solid block completely formed under the metal mesh. It can be seen from Fig. 14 that when the metal mesh positions were $Y$ = 60 mm and $Y$ = 180 mm, the interception rates $\varepsilon$ were only 11.4% and 13.5%, indicating that the metal mesh position had a significant influence on molten salt seepage blocking. When the metal mesh was close to the tank, it had a very weak blocking effect on molten salt seepage, mainly because the steady-state temperature at $Y$ = 60 mm was much higher than the freezing point of molten salt. It can be concluded that molten salt could not form solidified crystals at this position. Therefore, the metal mesh should be arranged whenever possible at a position with a lower foundation temperature, where the molten salt can undergo intense heat exchange with LECA and then solidify, so that the metal mesh can better block the molten salt. In other words, at the construction site, the metal mesh should not be placed too close to the bottom of the storage tank in the foundation.

#### 3.2.3. Effect of operating temperature on seepage and blocking

It can be seen from Fig. 6 that since the lower the operating temperature, the lower is the overall foundation temperature. If the metal mesh is arranged too far from the resistance heater, the molten salt may not be able to flow through the metal mesh, and therefore the mesh position $Y$ = 180 mm was selected. The effect of operating temperature $T_{op}$ on seepage characteristics is shown in Fig. 15, where the metal mesh aperture $S$ was 0.15 mm and the mass of leaked molten salt $M_{le}$ was 450 g. The values of $D_1$ in cases B2, C1, and C2 were 114, 58, and 53 mm respectively. This shows that when the temperature dropped to a certain extent, $D_1$ changed very little. The depths of molten salt seepage $D_2$ were 531, 456, and 341 mm when the operating temperature was 550 °C, 450 °C, and 350 °C, and the maximum seepage widths $W$ were 177, 243, and 269 mm. This was the case mainly because the operating

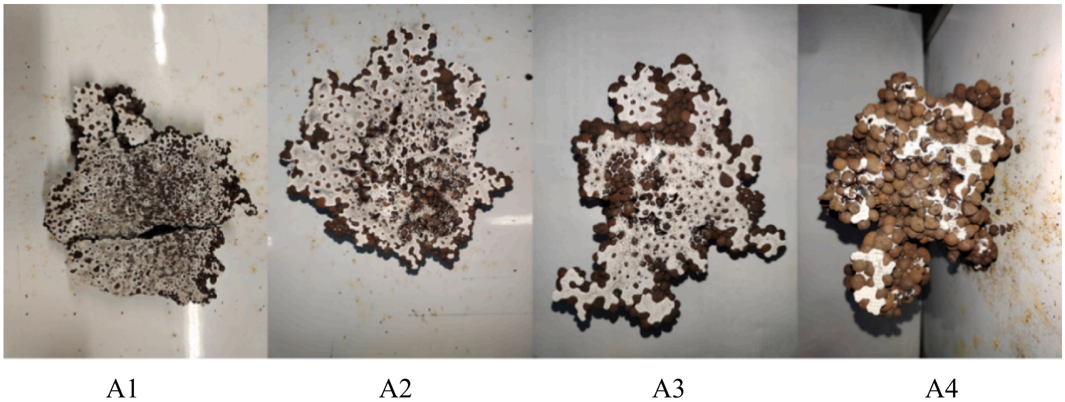


**Fig. 11.** Cross-sectional appearance of the metal mesh layer under different metal mesh apertures.

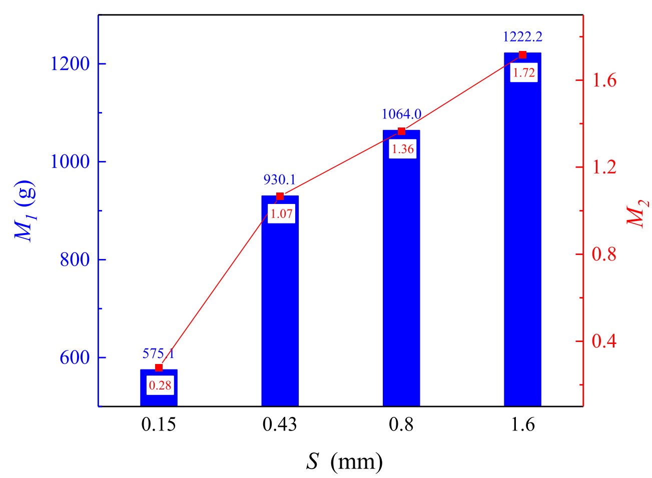


**Fig. 12.** Effect of metal mesh aperture on the mass of the solid block.

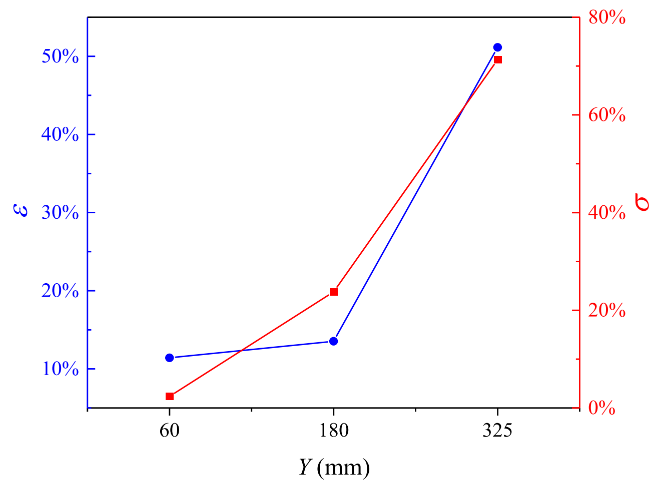


**Fig. 14.** Effect of metal mesh position on blocking of molten salt.

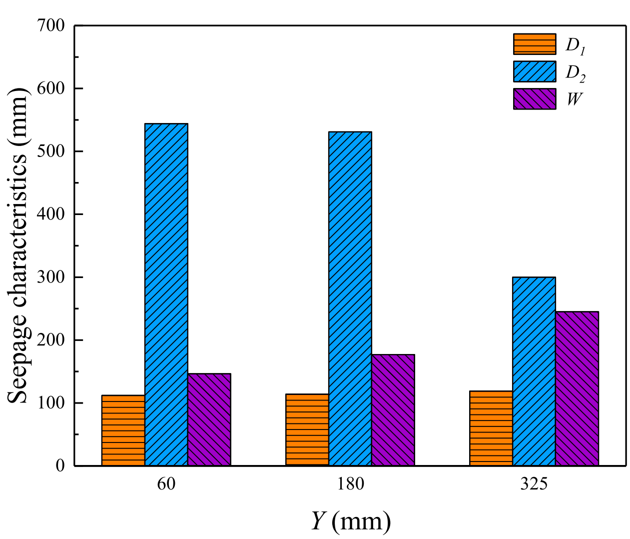


**Fig. 13.** Effect of metal mesh position on seepage characteristics.

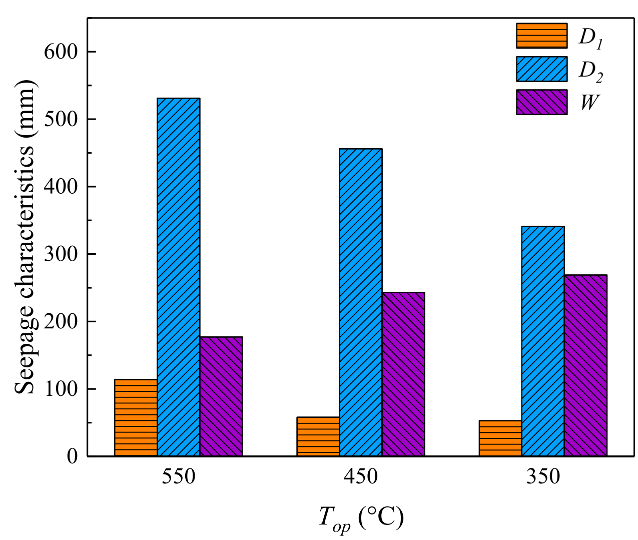


**Fig. 15.** Effect of operating temperature on the seepage characteristics.

temperature was low, the temperature of the upper layer of the tank foundation was also reduced, the position of the molten salt solidification zone was raised, and the seepage depth became less. At the same time, the molten salt solidification process dominates the whole process at the metal mesh position, and the maximum width is increased accordingly.

The solid block under the metal mesh is shown in Fig. 16. As $T_{op}$ decreased, the average width of the solid block under the metal mesh was significantly reduced. Clearly, the area where molten salt broke through the metal mesh was more concentrated in the center of the seepage. This occurred because when the operating temperature was

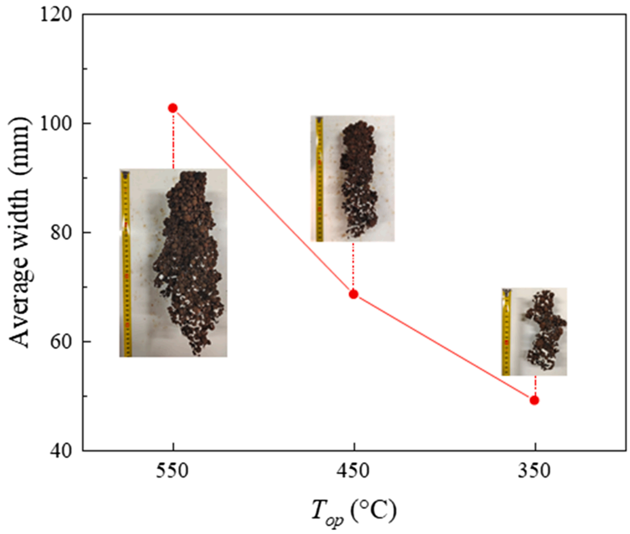


**Fig. 16.** Average width of the solid block under the metal mesh at different operating temperatures.

reduced and the molten salt penetrated the metal mesh and seeped along the radial direction of the foundation, it solidified and crystallized more easily, resulting in a decrease in the average width of the solid block under the metal mesh.

Fig. 17 shows the effect of operating temperature $T_{op}$ on the mass of the solid block. At $T_{op}$ values of 550 °C, 450 °C, and 350 °C, the masses of the solid block $M_1$ were 745.2 g, 647.9 g, and 441.5 g respectively, and $M_2$ were 1.6, 1.44, and 0.98 respectively. As the operating temperature decreased, the mass of LECA adsorbed per unit mass of molten salt $M_2$ diminished, mainly due to the lower operating temperature, which reduced the overall temperature of the foundation and made solidification of molten salt occur earlier. The seepage distance became shorter, and therefore less LECA was adsorbed along the way. Although a higher operating temperature of the molten salt in the tank can increase the maximum thermal storage power, it also increases the peak maximum mechanical stress (Wang et al., 2021) and aggravates tank corrosion. Moreover, a high operating temperature will also weaken the blocking ability of the metal mesh after molten salt leakage. A suggestion was made that the operating temperature of the storage tank in the power plant can be appropriately lowered for operating safety.

### 3.2.4. Effect of leaked mass of molten salt on seepage and blocking

Fig. 18 shows the effect of the leaked mass $M_{le}$ on the seepage characteristics of molten salt, where the operating temperature $T_{op}$ was 450 °C, the metal mesh aperture $S$ was 0.15 mm, and the metal mesh position $Y$ was 180 mm. At $M_{le}$ values of 450 g, 650 g, and 900 g, the molten salt seepage depths $D_2$ were 456, 481, and 679 mm respectively, and the maximum seepage widths $W$ were 243, 312, and 305 mm. The masses of the solid block $M_1$ were 1097.9, 1335.0, and 2348.8 g respectively. Note that as the leaked mass of molten salt increased, the depth of seepage also increased. However, when $M_{le}$ increased from 650 g to 900 g, the length of the solid block increased greatly, but the seepage width did not increase significantly. This shows that when $M_{le}$ increased substantially, the blocking effect of the metal mesh on the molten salt was not apparent. The molten salt broke through the metal mesh under the action of gravity, and the depth of seepage was significantly increased. Of course, this may also occur if the metal mesh position is not deep enough.

Fig. 19 shows a physical picture of solid blocks under the metal mesh. At $M_{le}$ of 450, 650, and 900 g, the lengths of the solid block under the metal mesh were 276, 301, and 499 mm. When $M_{le}$ increased from 450 g to 650 g, the length of the solid block under the metal mesh increased by 8.31%, but when $M_{le}$ increased from 450 g to 900 g, the length of the solid block under the metal mesh increased by 80.80%. This shows that when $M_{le}$ increased beyond a certain extent, the blocking effect of the metal mesh on molten salt leakage was reduced. In view of these results, this method of controlling the leakage range should be used in conjunction with molten salt leakage detection technology. When molten salt leakage is detected, the molten salt in the storage tank where the accident occurred should be quickly pumped into another intact storage tank. In this way, while reducing accident hazards, prompt action can also maximize the blocking effect of the metal mesh on leakage.

## 4. Conclusions

This article has presented an experimental study on leakage and seepage blocking in a molten salt storage tank foundation under different conditions. The results obtained are briefly summarized below:

(1) Leakage of molten salt significantly increases the steady-state axial temperature of the foundation because the thermal conductivity of the leaking molten salt is greater than that of the air among the foundation material granules.
(2) As the metal mesh aperture is reduced, the seepage depth decreases, and the maximum seepage width increases. The maximum interception rate and diffusion rate were 47.06% and 71.29% respectively. When the depth of metal mesh was increased from 60 mm to 325 mm, molten salt seepage depth decreased by 219 mm. Seepage depth decreased from 531 mm to

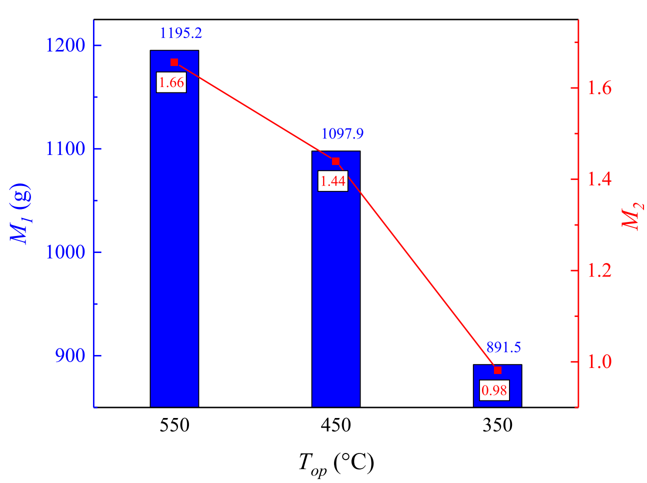


**Fig. 17.** Effect of operating temperature on the mass of the solid block.

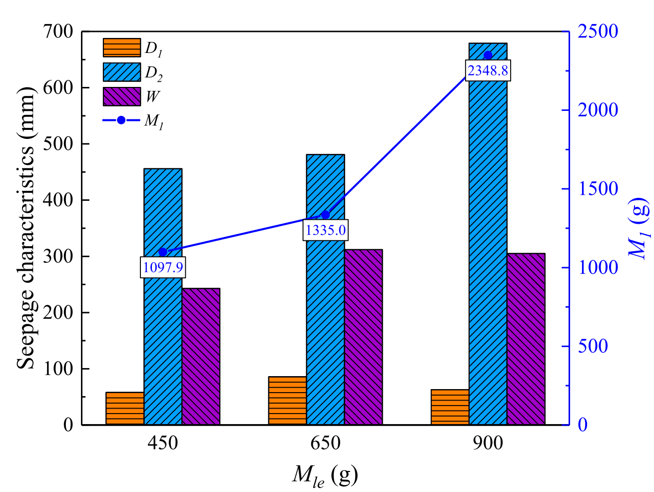


**Fig. 18.** Effect of leaked molten salt mass on the seepage characteristics.

C1 E1 E2

**Fig. 19.** Solid blocks under the metal mesh at different masses of leaked molten salt.

341 mm when operating temperature was lowered from 550 °C to 350 °C. Nonetheless, the blocking effect of the metal mesh on leakage was reduced when the mass of leaked molten salt increased from 450 g to 900 g.

(3) The metal mesh method for blocking molten salt leakage should be considered for application together with leakage detection technology in the storage tank foundation of a real solar power plant. At the same time, metal mesh with smaller aperture should be used, and the arrangement should be installed at some distance from the bottom of the storage tank. For safe operation, the molten salt temperature in the hot salt storage tank can be slightly reduced.

## Declaration of Competing Interest

The authors declare that they have no known competing financial interests or personal relationships that could have appeared to influence the work reported in this paper.

## Acknowledgements

This work was supported by National Natural Science Foundation of China (52036008).

## References

Bonilla, J., Rodríguez-García, M.M., Roca, L., de la Calle, A., Valenzuela, L., 2018. Design and experimental validation of a computational effective dynamic thermal energy storage tank model. Energy 152, 840–857. https://doi.org/10.1016/j.energy.2017.11.017.

Chieruzzi, M., Cerritelli, G.F., Miliozzi, A., Kenny, J.M., Torre, L., 2017. Heat capacity of nanofluids for solar energy storage produced by dispersing oxide nanoparticles in nitrate salt mixture directly at high temperature. Sol. Energy Mater. Sol. Cells 167, 60–69. https://doi.org/10.1016/j.solmat.2017.04.011.

Dunn, R.I., Hearps, P.J., Wright, M.N., 2012. Molten-salt power towers: Newly commercial concentrating solar storage. Proc. IEEE 100 (2), 504–515.

Feng, Q., Cha, L., Dai, C., Zhao, G., Wang, S., 2020. Effect of particle size and concentration on the migration behavior in porous media by coupling computational fluid dynamics and discrete element method. Powder Technol. 360, 704–714. https://doi.org/10.1016/j.powtec.2019.10.011.

Fernández, A.G., Lasanta, M.I., Pérez, F.J., 2012. Molten salt corrosion of stainless steels and low-Cr steel in CSP plants. Oxid. Met. 78, 329–348. https://doi.org/10.1007/s11085-012-9310-x.

Flueckiger, S., Yang, Z., Garimella, S.V., 2011. An integrated thermal and mechanical investigation of molten-salt thermocline energy storage. Appl. Energy 88, 2098–2105. https://doi.org/10.1016/j.apenergy.2010.12.031.

Gomes, A., Navas, M., Uranga, N., Paiva, T., Figueira, I., Diamantino, T.C., 2019. High-temperature corrosion performance of austenitic stainless steels type AISI 316L and AISI 321H, in molten Solar Salt. Sol. Energy 177, 408–419. https://doi.org/10.1016/j.solener.2018.11.019.

Huang, Y., Wang, P., Fu, Z., Shen, H., 2020. Experimental and numerical research on migration of LNAPL contaminants in fractured porous media. Hydrogeol. J. 28, 1269–1284. https://doi.org/10.1007/s10040-020-02118-w.

Juan lin, Shen, Y., Li, X., Hasnaoui, A., 2021. BRICS carbon neutrality target: Measuring the impact of electricity production from renewable energy sources and globalization. J. Environ. Manage. 298, 113460.

Kannan, N., Vakeesan, D., 2016. Solar energy for future world: - A review. Renew. Sustain. Energy Rev. 62, 1092–1105.

Lovegrove, K., Stein, W., 2021. In: Concentrating Solar Power Technology. Elsevier, pp. 3–17.

Peinado Gonzalo, A., Pliego Marugán, A., García Márquez, F.P., 2019. A review of the application performances of concentrated solar power systems. Appl. Energy. 255, 113893.

Price, H., Mehos, M., Kearney, D., Cable, R., Kelly, B., Kolb, G., Morse, F., 2021. Concentrating solar power best practices. Conc. Sol. Power Technol. 725–757 https://doi.org/10.1016/b978-0-12-819970-1.00020-7.

Qi, H.B., Li, D.H., Wei, W., Hu, X.H., Li, D., Wu, G.Z., Liu, X.Y., 2018. Lattice Boltzmann simulation of resistance coefficient of the oil and water migration in porous media. Therm. Sci. 22, 547–556. https://doi.org/10.2298/TSCI171011039Q.

Rodríguez, I., Pérez-Segarra, C.D., Lehmkuhl, O., Oliva, A., 2013. Modular object-oriented methodology for the resolution of molten salt storage tanks for CSP plants. Appl. Energy 109, 402–414. https://doi.org/10.1016/j.apenergy.2012.11.008.

Torras, S., Pérez-Segarra, C.D., Rodríguez, I., Rigola, J., Oliva, A., 2015. Parametric Study of Two-tank TES Systems for CSP Plants. Energy Procedia 69, 1049–1058.

Villada, C., Ding, W., Bonk, A., Bauer, T., 2021. Engineering molten MgCl2–KCl–NaCl salt for high-temperature thermal energy storage: Review on salt properties and corrosion control strategies. Sol. Energy Mater. Sol. Cells 232, 111344.

Wan, B., Tian, L., Fu, M., Zhang, G., 2021. Green development growth momentum under carbon neutrality scenario. J. Clean. Prod. 316, 128327.

Wan, Z., Wei, J., Qaisrani, M.A., Fang, J., Tu, N., 2020. Evaluation on thermal and mechanical performance of the hot tank in the two-tank molten salt heat storage system. Appl. Therm. Eng. 167, 114775.

Wang, G., Liu, Z., Han, W., Jiang, T., Chen, Z., 2021. Influence investigation of hot molten salt temperature on operation and mechanical behaviours of latent heat storage tank. Case Stud. Therm. Eng. 28, 101522 https://doi.org/10.1016/j.csite.2021.101522.

Wang, G., Yu, S., Niu, S., Chen, Z., Hu, P., 2020. A comprehensive parametric study on integrated thermal and mechanical performances of molten-salt-based thermocline tank. Appl. Therm. Eng. 170, 115010 https://doi.org/10.1016/j.applthermaleng.2020.115010.

Wang, J., Cai, Q., Chen, R., Xiao, X., Li, Y., Tian, W., Qiu, S., Su, G.H., 2022. Numerical analysis of melt migration and solidification behavior in LBR severe accident with MPS method. Nucl. Eng. Technol. 54 (1), 162–176. https://doi.org/10.1016/j.net.2021.07.043.

Wu, J., Ding, J., Lu, J., Wang, W., 2017. Migration and phase change phenomena and characteristics of molten salt leaked into soil porous system. Int. J. Heat Mass Transf. 111, 312–320. https://doi.org/10.1016/j.ijheatmasstransfer.2017.04.002.

Zhang, X., Zhang, C., Wu, Y., Lu, Y., 2020. Experimental research of high temperature dynamic corrosion characteristic of stainless steels in nitrate eutectic molten salt. Sol. Energy 209, 618–627. https://doi.org/10.1016/j.solener.2020.09.034.

Zhang, Y., Wu, J., Wang, W., Ding, J., Lu, J., 2019. Experimental and numerical studies on molten salt migration in porous system with phase change. Int. J. Heat Mass Transf. 129, 397–405. https://doi.org/10.1016/j.ijheatmasstransfer.2018.09.122.

Zhou, H., Shi, H., Lai, Z., Zuo, Y., Hu, S., Zhou, M., 2020a. Migration and phase change study of leaking molten salt in tank foundation material. Appl. Therm. Eng. 170, 114968.

Zhou, H., Shi, H., Zhang, J., Zhou, M., 2020b. Experimental and numerical investigation of temperature distribution and heat loss of molten salt tank foundation at different scales. Heat Mass Transf. 56, 2859–2869. https://doi.org/10.1007/s00231-020-02905-x.

Zhou, H., Wang, Z., Zhou, M., Cen, K., 2019. Experimental measurements and XCT based simulation of effective thermal conductivity of stacked ceramsites in molten-salt tank foundation. Heat Mass Transf. 55, 3103–3115. https://doi.org/10.1007/s00231-019-02646-6.

Zhou, H., Wang, Z., Zhou, M., Xu, J., 2020c. Thermal properties, permeability and compressive strength of highly porous accumulated ceramsites in the foundation of salt tank for concentrate solar power plants. Appl. Therm. Eng. 164, 114451.